

Article

Geochronology and Stable Isotope Analysis of Fracture-Fill and Karst Mineralization Reveal Sub-Surface Paleo-Fluid Flow and Microbial Activity of the COSC-1 Borehole, Scandinavian Caledonides

Henrik Drake ^{1,*} , Nick M. W. Roberts ²  and Martin J. Whitehouse ³¹ Department of Biology and Environmental Science, Linnæus University, 39182 Kalmar, Sweden² Geochronology and Tracers Facility, British Geological Survey, Nottingham NG12 5GG, UK; nirob@bgs.ac.uk³ Swedish Museum of Natural History, 114 18 Stockholm, Sweden; martin.whitehouse@nrm.se

* Correspondence: henrik.drake@lnu.se

Received: 13 December 2019; Accepted: 27 January 2020; Published: 3 February 2020



Abstract: The deep biosphere hosted in fractured rocks within the upper continental crust is one of the least understood and studied ecological realms on Earth. Scarce knowledge of ancient life and paleo-fluid flow within this realm is owing to the lack of deep drilling into the crust. Here we apply microscale high spatial-resolution analytical techniques to fine-grained secondary minerals in a deep borehole (COSC-1) drilled into the Silurian-Devonian Scandinavian Caledonide mountain range in central Sweden. The aim is to detect and date signs of ancient microbial activity and low-temperature fluid circulation in micro-karsts (foliation-parallel dissolution cavities in the rock) and fractures at depth in the nappe system. Vein carbonates sampled at 684 to 2210 m show a decreased C isotope variability at depths below 1050 m; likely due to decreased influence of organic-C at great depth. Micro-karsts at 122–178 m depth feature at least two generations of secondary calcite and pyrite growth in the voids as shown by secondary ion mass spectrometry analytical transects within individual grains. The younger of these two precipitation phases shows ³⁴S-depleted $\delta^{34}\text{S}_{\text{pyrite}}$ values ($-19.8 \pm 1.6\text{‰}$ vs. Vienna-Canyon Diablo Troilite (V-CDT)) suggesting microbial sulfate reduction in situ. The calcite of this late phase can be distinguished from the older calcite by higher $\delta^{18}\text{O}_{\text{calcite}}$ values that correspond to precipitation from ambient meteoric water. The late stage calcite gave two separate laser ablation inductively coupled mass spectrometry-derived U-Pb ages (9.6 ± 1.3 Ma and 2.5 ± 0.2 Ma), marking a minimum age for widespread micro-karst formation within the nappe. Several stages of fluid flow and mineral precipitation followed karst formation; with related bacterial activity as late as the Neogene-Quaternary; in structures presently water conducting. The results show that our combined high spatial-resolution stable isotope and geochronology approach is suitable for characterizing paleo-fluid flow in micro-karst; in this case, of the crystalline crust comprising orogenic nappe units.

Keywords: in situ U-Pb geochronology; secondary minerals; stable isotopes; Caledonides; deep drilling (COSC-1)

1. Introduction

Fluid circulation and mixing in fractures and during vein formation can lead to metal leaching and accumulation of ores, such as those in the Harz mountains, Germany [1]. Microbial activity in fractured rock volumes can also be of importance for ore-forming processes [2,3] and may involve potentially significant microbial natural gas accumulations [4,5]. Furthermore, microbial activity and fluid flow may involve important redox processes and fluctuations that are relevant for safety

assessments of repositories for toxic wastes such as spent nuclear fuel [6,7]. Knowledge of ancient microbial processes and fluid flow in the upper crust can, therefore, have wide-ranging implications. Information about these processes can be preserved as diagnostic isotope signatures within authigenic minerals over geological timescales, for instance as excursions in $^{13}\text{C}/^{12}\text{C}$ ($\delta^{13}\text{C}$) in carbonate due to methane oxidation or formation [8–11] as well as excursions in $^{34}\text{S}/^{32}\text{S}$ ($\delta^{34}\text{S}$) in sulfides due to microbial sulfate reduction (MSR) [12–14]. These isotopic markers are related to the fractionation that occurs during microbial metabolisms, at degrees that are beyond what abiotic sources and thermochemical reactions produce [15,16]. In addition, the $^{18}\text{O}/^{16}\text{O}$ composition ($\delta^{18}\text{O}$) of the carbonate can reveal origins of fluids [6,17,18] owing to the fact that the O isotope composition is a conservative tracer for different water types [19], when temperature-related fractionation during calcite formation has been considered [20–22].

In deep granitoid fractures of the Fennoscandian Shield in eastern Sweden (Laxemar and Forsmark sites) and western Finland (Olkiluoto, Figure 1), several recent studies have applied micro-scale secondary ion mass spectrometry (SIMS) techniques to fine-grained secondary low-temperature calcite and pyrite mineral coatings, revealing several discrete events of microbial-related mineral precipitation [14,23–27]. The isotopic variability for both $\delta^{34}\text{S}$ (−54‰ to +132‰ V-CDT, Vienna-Canyon Diablo Troilite reference value) and $\delta^{13}\text{C}$ (−125‰ to +37‰ V-PDB, Vienna-Pee Dee Belemnite reference value) [14,28,29], is beyond what has been reported from other settings. At Forsmark, U-Pb carbonate geochronology using laser-ablation inductively coupled mass spectrometry (LA-ICP-MS) was successfully applied to calcite with anaerobic oxidation of methane-related (^{13}C -depleted) composition, revealing a Jurassic age [28]. In the fractured Devonian impact structure at Siljan, central Sweden, U-Pb dating was used to constrain dominantly Eocene–Miocene ages of secondary calcite formed following microbial methanogenesis and methane oxidation [5].

Here we use the aforementioned high spatial resolution isotopic and geochronological techniques to decipher low-temperature fluid circulation and to trace ancient microbial activity within a single deep borehole. The COSC-1 borehole is part of the Collisional Orogeny in the Scandinavian Caledonides (COSC) project, part-funded through the International Continental Drilling Project (ICDP). COSC focuses on mountain-building processes in a major mid-Paleozoic orogen in western Scandinavia and its comparison with modern analogues [30,31]. The deep borehole and core, with ~2.5 km at ~100% recovery, offers an excellent opportunity for geophysical and geochemical characterization of the crystalline crust. For the Scandinavian Caledonides, extensive characterization exists for tectonics of the nappe units [32,33] and for denudation and uplift [34,35], but knowledge of low-temperature fluid circulation and microbial activity in the deep fracture systems of the nappes is non-existent. Secondary mineral investigations of Caledonide-related hydrothermal brine-type mineralizations have been carried out, such as at Laisvall, Vassbo and Osen, but these mineralizations are temporally very close to the Caledonide orogenic event itself [36]. The preliminary borehole investigations of COSC-1 have shown that there are several micro-karst horizons formed within carbonate-rich layers of the gneisses, as well as abundant calcite veins [30,37,38], which both enable studies of low-temperature mineral formation and consequently of fluid circulation and ancient microbial activity. This study of secondary carbonate and sulfide mineralization in deep micro-karsts and veins of the COSC-1 core aims to increase our understanding of low-temperature fluid circulation and microbial activity in the nappe system of an ancient orogeny.

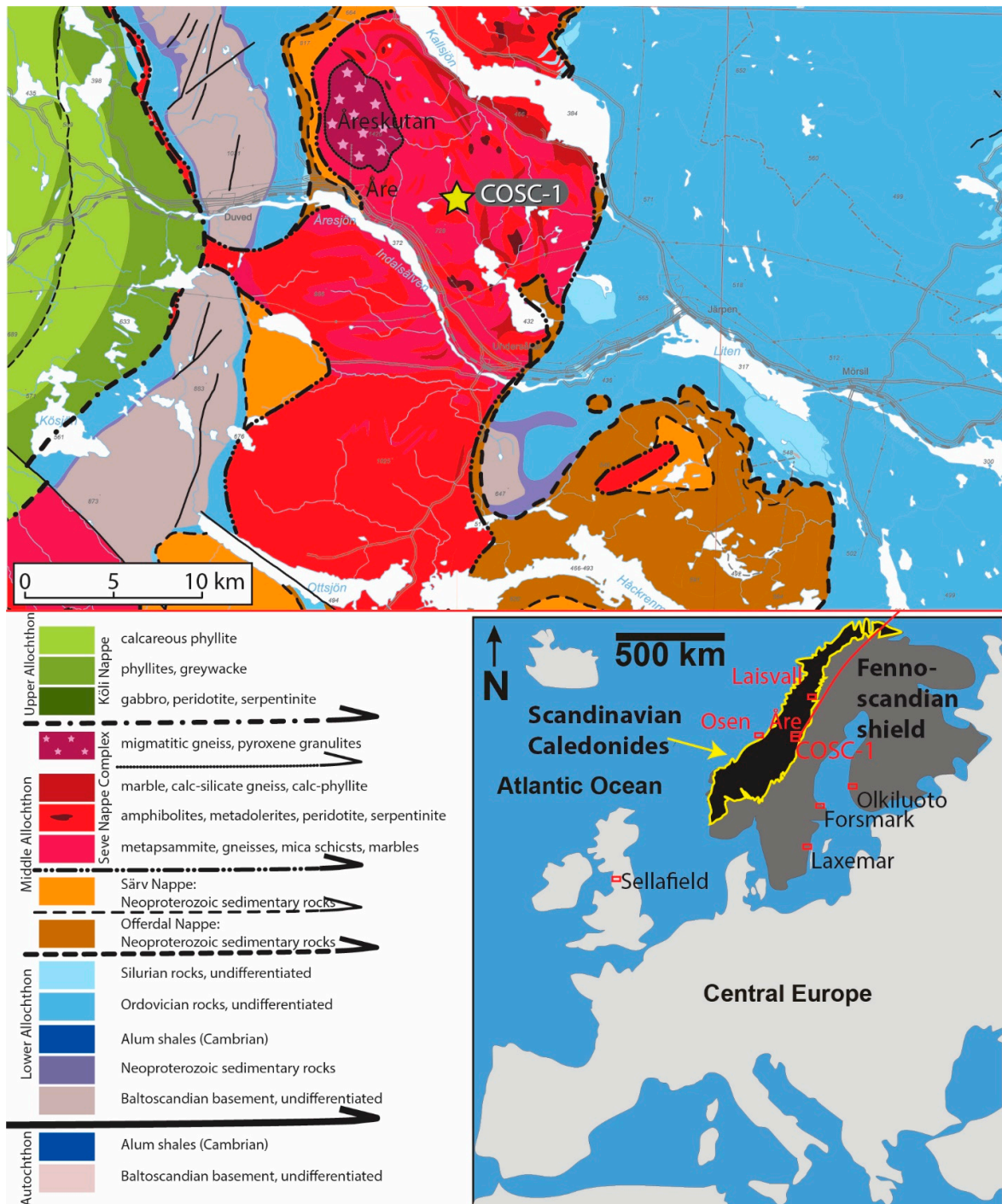


Figure 1. Geological map of the study area and the location of the COSC-1 (Collisional Orogeny in the Scandinavian Caledonides) borehole (yellow star symbol marks surface location, at coordinates 63°24' N, 13°5' E) along with information about the thrust sheets. Modified from Lorenz et al., [30,38]. Sites of previous geochemical and geobiological studies in fractures and veins are also indicated.

2. Geological Setting and the COSC-1 (Collisional Orogeny in the Scandinavian Caledonides) Borehole

The COSC-1 borehole was drilled in 2014 and is a ca. 2.5 km deep (2495.8 m), cored drill hole located close to the town of Åre in Jämtland, central Sweden (Figure 1). It targeted a thick section of the lower part of the Seve Nappe Complex and was planned to penetrate its basal thrust zone

into the underlying lower-grade metamorphosed allochthon, but drilling did not reach that planned horizon [30].

The Caledonides of western Scandinavia and eastern Greenland formed as the result of a set of events that started with the closure of the Iapetus Ocean during the Ordovician, and subsequent underthrusting of continent Laurentia by Baltica in the Silurian and Early Devonian during the Scandian collisional orogenic stage. The allochthons were subjected to high-grade metamorphism and emplaced onto the adjacent platforms by eastward thrust emplacement by up to several hundred kilometres [33]. In central Sweden, the thrust sheets are divided into the Lower, Middle, Upper and Uppermost allochthons [39] that are unconformably overlying the Proterozoic crystalline basement, as marked by a front thrust sheet that dips 1–2° to the west [31]. Sedimentary successions of Neoproterozoic and Cambro-Silurian strata dominate the Lower Allochthon (Jämtlandian Nappes). The overlying Middle Allochthon is of higher metamorphic grade and contains a basal basement-derived thrust sheet, overlain by Offerdal Nappe metasandstones, and the Särvi Nappe [40,41]. The Seve Nappe Complex is the uppermost tectonic unit in the Middle Allochthon and has a lower part that has experienced ductile deformation in dominantly amphibolite facies; a central part (e.g., Åreskutan Nappe) of migmatites and paragneisses and an upper, amphibolite-dominated unit [42]. Absolute ages reported from migmatite and associated rocks of the Åreskutan mountain 6 km to the west of the COSC-1 borehole are in the range of c. 455 to 420 Ma [43–47]. The Köli Nappes in the Upper Allochthon are the tectonostratigraphically highest rocks in study area (Figure 1). This unit is dominated by sedimentary rocks of Early Paleozoic age, and has experienced greenschist facies [42]. The Uppermost Allochthon contains metasedimentary rocks of inferred Laurentian margin origin, but are not present in the study area.

The drilling of the COSC-1 borehole aimed to study mountain building processes at mid-crustal levels in a major orogen, with a focus on the Seve Nappe Complex. The borehole lithology is briefly described in Figure S1 and, according to Lorenz et al., [30,38], the core has the following characteristics: the upper 1800 m is dominated by gneisses of varying compositions (e.g., felsic, amphibole, Calcium silicate) belonging to the Lower Seve Nappes. Highly strained metagabbros and amphibolites are common, and marbles, pegmatite dykes and minor mylonites also occur. Fractures that are interpreted to be of young, i.e., post-orogen, age are sparse. A water-conducting set of very steep fractures has resulted in dissolution of bands in the gneisses to form foliation parallel micro-karst (e.g., at about 175 m and between 1200 and 1320 m). Narrow deformation bands and mylonites mark the first signs of increasing strain below 1700 m. The base of the Seve nappes was interpreted to be at c. 2000–2100 m [37]. Below 2100 m, mylonites dominate. The lower part of the drill core is dominated by mylonitized quartzites and metasandstones of unclear tectonostratigraphic position that are mylonitized to varying degrees. A set of hydrological tests run during the drilling campaign revealed the location of likely water-conductive fractures between the tested depth range of 300–2500 m, these occurred at 339, 507, 554, 696, 1214, 1245, 2300 and 2380 m [48]. Borehole temperature profiling suggest a geothermal gradient of ~20 °C km⁻¹ with temperatures reaching almost 55 °C in the bottom of the hole [30].

3. Materials and Methods

Eight samples containing secondary minerals (carbonate ± sulfides) were collected from the COSC-1 borehole core (core log with samples marked in Supplementary Figure S1). The samples were cut into thick polished blocks and analyzed with a petrographic microscope and scanning electron microscope (SEM). Micro-karst samples were analyzed directly in the drill core specimen and euhedral calcite and pyrite crystals were hand-picked from the karst voids and embedded in epoxy. These epoxy grain mounts were polished to expose a cross section of the crystals, and the interiors of these crystals were targeted with SIMS analysis for stable C, O, (calcite) and S (pyrite) isotopes and with LA-ICP-MS for U-Pb geochronology (calcite) after SEM-documentation of zonations and impurities.

3.1. Scanning Electron Microscopy (SEM)

The mineralogy and appearance of the uncoated fracture coatings and rock chips of veins were examined under low-vacuum conditions in a Hitachi S-3400N scanning electron microscope (SEM) equipped with an integrated energy-dispersive spectroscopy (EDS) system. The coatings were then scraped off for analyses of stable isotopes and U-Pb geochronology.

3.2. Secondary Ion Mass Spectrometry for $\delta^{13}\text{C}$, $\delta^{18}\text{O}$, $\delta^{34}\text{S}$

Intra-crystal SIMS-analysis (10 μm lateral beam dimension, 1–2 μm depth dimension) of sulfur isotopes in pyrite and carbon and oxygen isotopes in calcite was performed on a Cameca IMS1280 ion microprobe at the NordSIM facility at the Museum of Natural History, Stockholm, Sweden, following the analytical settings and tuning reported previously [14,29,49]. Sulfur was sputtered using a $^{133}\text{Cs}^+$ primary beam with 20 kV incident energy (10 kV primary, –10 kV secondary) and a primary beam current of ~1.5 nA. A normal incidence electron gun was used for charge compensation. Analyses were performed in automated sequences, with each analysis comprising a 70 second pre-sputter to remove the gold coating over a rastered $15 \times 15 \mu\text{m}$ area, centering of the secondary beam in the field aperture to correct for small variations in surface relief, and data acquisition in 16 four-second integration cycles. The magnetic field was locked at the beginning of the session using a nuclear magnetic resonance (NMR) field sensor. Secondary ion signals for ^{32}S and ^{34}S were detected simultaneously using two Faraday detectors with a common mass resolution of 4860 ($M/\Delta M$). Data were normalized for instrumental mass fractionation using matrix matched reference materials which were mounted together with the sample mounts and analyzed after every sixth sample analysis. Results are reported as per mil (‰) $\delta^{34}\text{S}$ based on the V-CDT reference value [50]. Analytical transects of up to ten spots were made from core to rim in the crystals. In total, 89 analyses were made for $\delta^{34}\text{S}$ of pyrite from 11 crystals from three fracture samples. The pyrite reference material S0302A with a conventionally determined value of $0.0\text{‰} \pm 0.2\text{‰}$ (R. Stern, University of Alberta, pers. comm.) was used. Typical precision on a single $\delta^{34}\text{S}$ value, after propagating the within run and external uncertainties from the reference material measurements was $\pm 0.07\text{‰}$.

For calcite, a total number of 84 $\delta^{13}\text{C}$ and 93 for $\delta^{18}\text{O}$ SIMS-analyses were performed on the same Cameca IMS1280 described above. Settings follow those described for S isotopes, with some differences: O was measured on two Faraday cups (FC) at mass resolution 2500, C used a FC/Electron Multiplier combination with mass resolution 2500 on the ^{12}C peak and 4000 on the ^{13}C peak to resolve it from $^{12}\text{C}^1\text{H}$. Calcite results are reported as per mil (‰) $\delta^{13}\text{C}$ based on the Pee Dee Belemnite (V-PDB) reference value. Analyses were carried out running blocks of six unknowns bracketed by two standards. Analytical transects of up to nine spots were made from core to rim in the crystals. Up to five crystals were analyzed from each fracture sample. Analyses were made for 31 crystals from 8 fracture samples. Isotope data from calcite were normalized using calcite reference material S0161 from a granulite facies marble in the Adirondack Mountains, kindly provided by R.A. Stern (Univ. of Alberta). The values used for instrumental mass fractionation correction were determined by conventional stable isotope mass spectrometry at Stockholm University on ten separate pieces, yielding $\delta^{13}\text{C} = 0.22\text{‰} \pm 0.35\text{‰}$ V-PDB (1 std. dev.) and $\delta^{18}\text{O} = -5.62\text{‰} \pm 0.22\text{‰}$ V-PDB (1 std. dev.). Precision was $\delta^{18}\text{O}$: $\pm 0.2\text{‰} - 0.3\text{‰}$ and $\delta^{13}\text{C}$: $\pm 0.4\text{‰} - 0.5\text{‰}$. Values of the reference material measurements are listed together with the samples in Supplementary Table S1 ($\delta^{13}\text{C}$), Table S2 ($\delta^{18}\text{O}$), and Table S3 ($\delta^{34}\text{S}$).

3.3. Laser Ablation Inductively Coupled Plasma Mass Spectrometry (LA-ICP-MS) for U-Pb Geochronology

U-Pb geochronology via the in situ LA-ICP-MS method was conducted at the Geochronology and Tracers Facility, British Geological Survey (Nottingham, UK). The method utilizes a New Wave Research 193UC excimer laser ablation system, coupled to a Nu Instruments Attom single-collector sector-field ICP-MS. The method follows that previously described in [51], and involves a standard-sample bracketing with normalization to NIST 614 silicate glass for Pb-Pb ratios and WC-1 carbonate for U-Pb

ratios. The laser parameters comprise a 80 μm static spot, fired at 10 Hz, with a $\sim 6 \text{ J/cm}^2$ fluence, for 20 s of ablation. Material is pre-ablated to clean the sample site with 120 μm spots for 2 s. No common lead correction is made; ages are determined by regression and the lower intercept on a Tera-Wasserburg plot (using Isoplot 4.15; [52]). Duff Brown, a carbonate previously measured by isotope dilution mass spectrometry was used as a validation, and pooling of all sessions yields a lower intercept age of $64.2 \pm 1.6 \text{ Ma}$ (MSWD = 4.0), overlapping the published age of $64.04 \pm 0.67 \text{ Ma}$ [53]. All ages are plotted and quoted at 2σ and include propagation of systematic uncertainties according to the protocol described in Horstwood et al., [54]. Data are screened for low Pb and low U counts below detection, and very large uncertainties on the Pb-Pb and Pb-U ratios which indicate mixed analyses. The spots are also checked after ablation for consistent ablation pit shape, and data are rejected if the ablations were anomalous (this results from material cleaving off, or clipping the resin mount).

Eight samples of calcite were screened from the COSC-1 drill core, but only one sample yielded measurable radiogenic lead. This sample (178 m) yielded variably robust U-Pb ages in the first session (based on the SIMS-analyzed crystals), and so a second session was added to this dataset using further mounted crystals. Full analytical data from the sessions are listed in Supplementary Table S4).

4. Results

4.1. Mineralogy

Mineralogical composition was characterized in eight samples, three from micro-karst (122, 122.8, 178 m) and five from deeper veins (684, 743, 1051, 1369, 2210 m). The micro-karst samples were investigated in the SEM in the karst cavities of the porous rocks in cut-off rock chips. The deeper veins were studied in the SEM as polished blocks (Figure 2).

4.1.1. Micro-Karst

The micro-karsts occurred as foliation parallel cavities in the gneiss (Figure 2a,c, Supplementary Table S5) and contained secondary fine-grained euhedral (rhombohedral) calcite crystals of up to 400 μm in size (Figure 2b,d) that line the walls of the micro-karst cavities. The calcite crystals commonly occur in aggregates of several equant crystals (see also Figure S2a–d). No growth zonations or overgrowths are evident based on the observation of morphology of the crystals in situ within the voids. Subhedral to euhedral pyrite crystals of up to 400 μm size occur together with calcite in the karst voids (Figure 2b,d). In sample 178 m, the zeolite chabazite is abundant, as euhedral blocky crystals of up to 1 mm in size (Figure 2d, Figure S2b–d). Chabazite is commonly intergrown with calcite. Albite and radiating aggregates of platy clay mineral crystals (Figure S2d) are occasionally present, and very fine-grained Ni-rich grains, which have detectable amounts of C, P and Si (EDS-analysis). Fine-grained C-rich filaments occur, particularly in sample 122.8, but also in sample 178 m (see SEM-images in Supplementary Figure S3). The polished calcite cross sections from the micro-karst revealed only scattered single-phased inclusions.

4.1.2. Veins

The sampled calcite veins were 1–10 mm in width (Figure 2e,g, more sample photos are shown in Supplementary Table S6), and occur both as individual veins and as breccias with calcite cement and wall rock fragments. Apart from calcite, the veins contain quartz, albite, chlorite and sulfides (pyrite and/or pyrrhotite) (Figure 2e–h). In sample 1051, albite lines the fracture and calcite is in the vein center. In sample 684, dolomite is abundant together with calcite (Figure 2f). Talc, pyrite and Ti-oxide (Figure S2e) also occur in this sample intergrown with the carbonates, suggesting formation of this mineral assemblage at a single event. There is also a younger calcite-talc filled micro-vein running along the edge of the main vein of this sample. Ca-Al-silicates occur in two samples, as epidote in sample from 1369 m occurring together with quartz (lining the fracture), calcite and pyrrhotite (Figure S2g), and as laumontite in sample from 743 m, where it is intergrown with calcite (Figure S2f). The deepest

sample (2210 m) holds secondary rare earth element (REE)-carbonate and ilmenite, intergrown with albite (Figure S2h). See Supplementary Tables S5 and S6 for detailed sample descriptions.

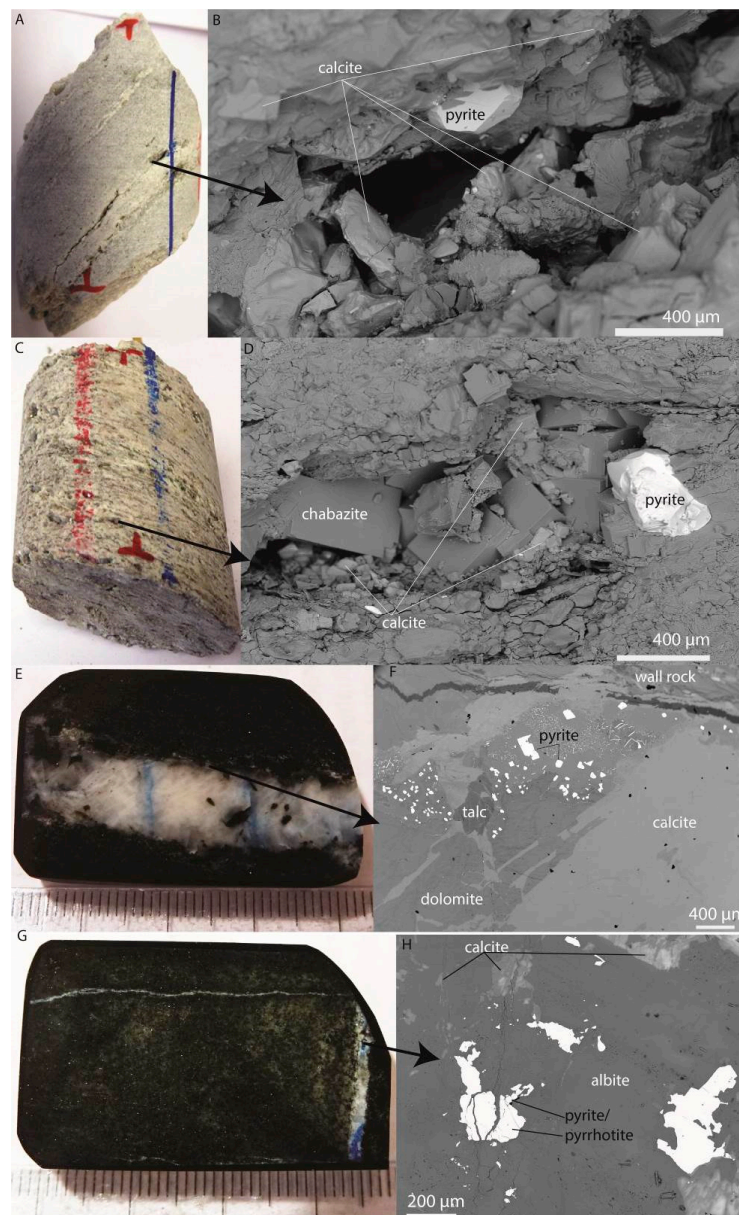


Figure 2. Mineral characteristics in photographed drill core samples (left) and back-scattered scanning electron microscope (SEM) images (right). (A–B): sample 122, micro-karst, showing secondary calcite and pyrite in a cavity. (C–D): sample 178, micro-karst, showing secondary chabazite, calcite and pyrite in a cavity. (E–F) calcite vein that also holds dolomite, talc and pyrite, sample 684. (G–H) vein with abundant albite, calcite and sulfides (intergrown pyrite and pyrrhotite), sample 1051.

4.2. Stable Isotopes

Calcite shows stable isotope compositions of $\delta^{18}\text{O}$: -28.9‰ to -10.7‰ V-PDB (span 18.2‰ , $n_{\text{spots}} = 93$, $n_{\text{samples}} = 8$) and $\delta^{13}\text{C}$: -17.4‰ to -3.5‰ V-PDB (span 13.9‰ , $n_{\text{spots}} = 84$, $n_{\text{samples}} = 8$). The karst calcite generally shows different populations of C and O isotope composition than the calcite veins (Figure 3a). The veins generally have depleted $\delta^{18}\text{O}$ values, mainly lighter than -22‰ (Figure 3b), and $\delta^{13}\text{C}$ values that are quite invariable at $-8\text{‰} \pm 1\text{‰}$ V-PDB in the two deepest samples and a larger

variability in the three shallowest veins (-17‰ to -5‰ V-PDB Figure 3c). The shallow veins also show larger spans in $\delta^{18}\text{O}$ than the deeper two (Figure 3b).

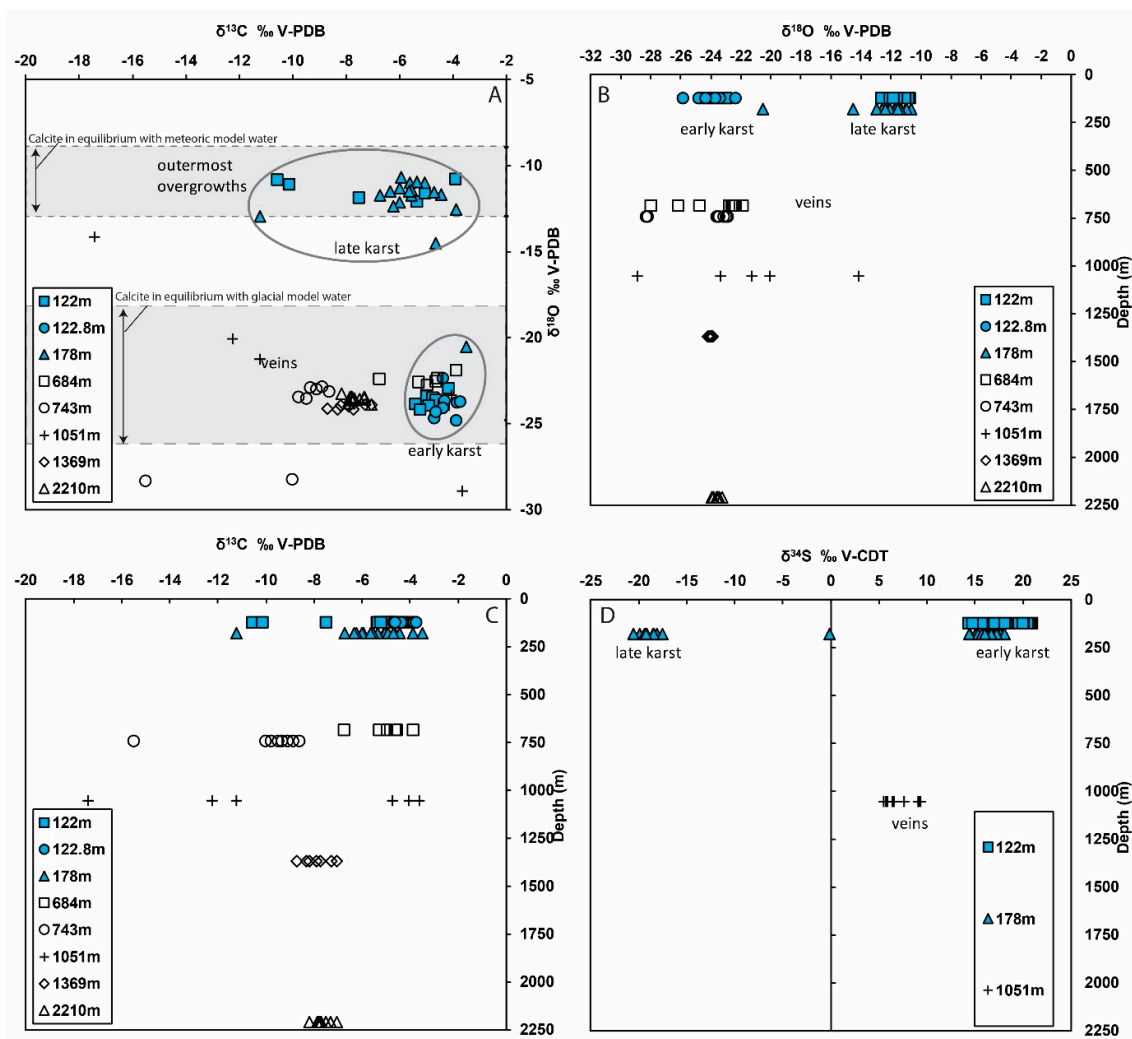


Figure 3. Stable isotope scatter and depth plots, divided into micro-karst samples (blue symbols) and vein samples (transparent symbols and black crosses). (A) $\delta^{18}\text{O}_{\text{calcite}}$ vs. $\delta^{13}\text{C}_{\text{calcite}}$, with marker for the different micro-karst groups (spheres), as well as spans of calculated values for hypothetical calcite precipitated from ambient meteoric or glacial water. For this comparison, temperature dependent fractionation factors for calcite precipitation at ambient temperatures are used for $\delta^{18}\text{O}$ [22]. See text for details of temperatures and isotope spans of the model waters. (B) $\delta^{18}\text{O}_{\text{calcite}}$ vs. depth. (C) $\delta^{13}\text{C}_{\text{calcite}}$ vs. depth. (D) $\delta^{34}\text{S}_{\text{pyrite}}$ vs. depth.

Two main groups of micro-karst calcite are evident, particularly manifested by the $\delta^{18}\text{O}$ composition, which shows a cluster at -25‰ to -20‰ V-PDB with most values below -22.5‰ , and one cluster with heavier values, at -14.5‰ to -10.8‰ V-PDB, with most values between -13‰ and -11‰ . The latter group occurs in samples 122 and 178, but not in sample 122.8 (Figure 3a). In sample 178, the isotopically heavy $\delta^{18}\text{O}$ values dominate. There is petrographic evidence for a temporal trend in the $\delta^{18}\text{O}$ values. The isotopically light $\delta^{18}\text{O}$ group is older than the isotopically heavier group as shown in Figure 4 where the core of the crystals is ^{18}O -poor compared to the later growth zone(s). In sample 122, the relatively ^{18}O -rich overgrowths make up very small parts of the crystal volume (Figure 4a–d), in contrast to in sample 178 where most of the crystal volume is made up of the ^{18}O -rich younger calcite (Figure 4e,f). The outermost overgrowth in sample 122 (with high Back Scattered Electron-intensity, Figure 4a,c) features a significant decrease in ^{13}C compared to the

other parts (Figure 4b,d). This means that three generations are observed within the calcite in the micro-karst (1: early karst, 2: late karst, 3: outermost overgrowth of late karst calcite, Figure 3a). A similar overgrowth occurs in sample 178 ($\delta^{13}\text{C}$: -11.2‰), but only in one spot, showing that the second calcite group dominated this sample.

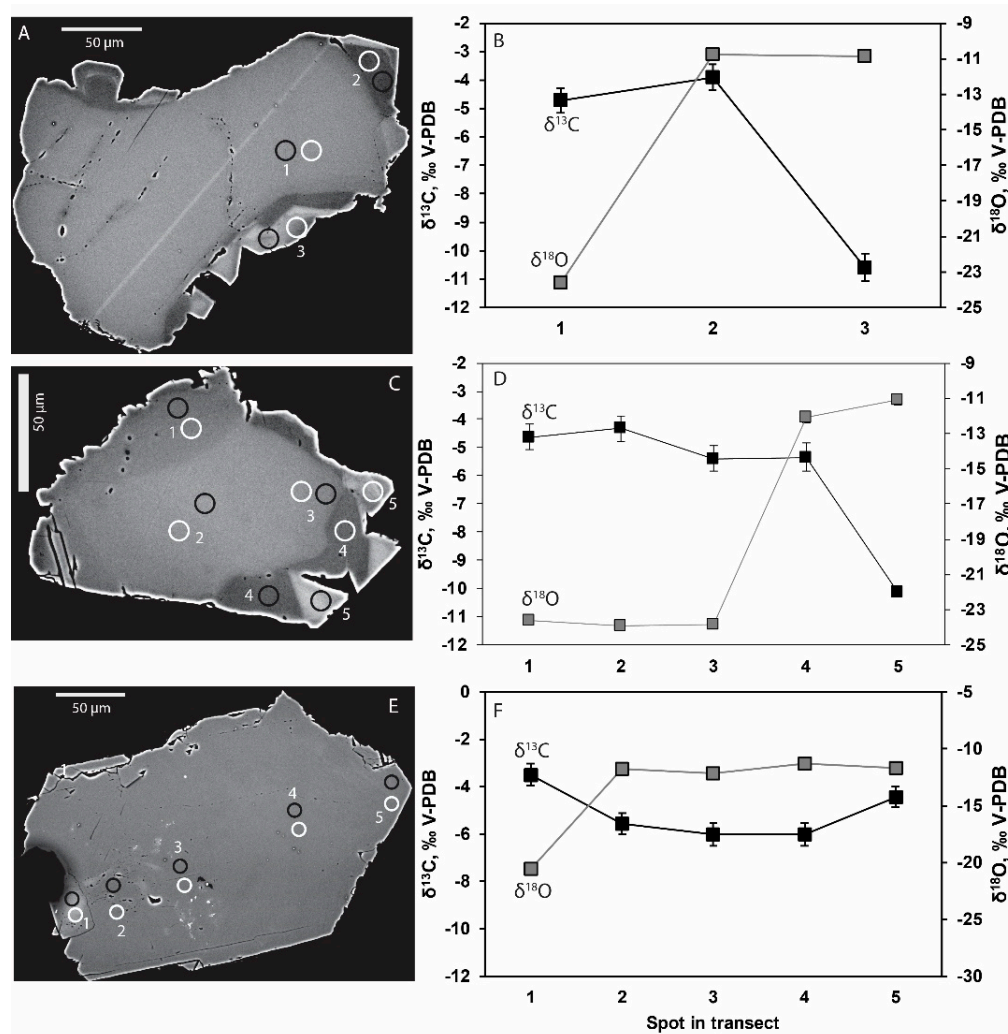


Figure 4. Microanalytical secondary ion mass spectrometry (SIMS) transects within calcite. Back scattered electron images of polished crystal cross sections are shown to the left (A,C,E) with spot locations indicated, for closely spaced 10 μm $\delta^{13}\text{C}$ (black) and $\delta^{18}\text{O}$ (white) SIMS spots. Corresponding isotopic values are shown on the graphs in B (sample 122 m), D (122 m), and F (178 m).

Pyrite shows $\delta^{34}\text{S}$ compositions ranging from -20.5‰ to $+20.9\text{‰}$ V-CDT (span 41.4‰ , $n_{\text{spots}} = 89$, $n_{\text{samples}} = 3$). Two samples show very narrow span, vein 1051 m: $7.8\text{‰} \pm 1.6\text{‰}$ and micro-karst 122 m: $18.8\text{‰} \pm 2.2\text{‰}$. The karst sample 178 m shows two distinct groups ($-19.8\text{‰} \pm 1.6\text{‰}$ and $+16.4\text{‰} \pm 1.0\text{‰}$) and one value in between (-0.1‰), of which the isotopically heaviest group overlaps with micro-karst sample 122 m. Petrographically, the isotopically heavy pyrite in sample 178 m is oldest, as it is found in the inner part of a crystal with an isotopically light rim (Figure 5a). The same sample also features pyrite crystals having both light values throughout the whole crystal (Figure 5B) as well as heavy values throughout the whole crystal (Table S3). The isotopically light pyrite is coeval with the calcite zonation group “late karst” with $\delta^{13}\text{C}$ values of -7‰ to -3‰ .

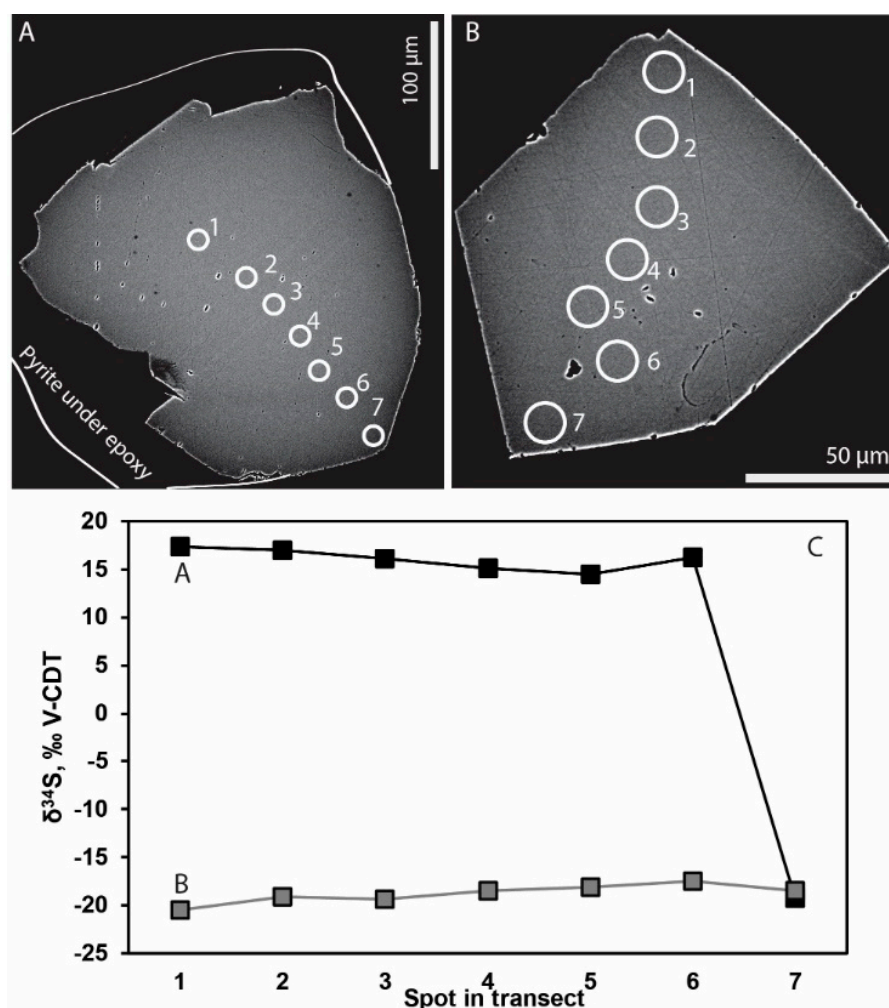


Figure 5. Microanalytical SIMS $\delta^{34}\text{S}$ transects within pyrite. Back Scattered Electron images of polished crystal cross sections are shown in **A** and **B** with spot locations indicated, for closely spaced 10 μm $\delta^{34}\text{S}$ SIMS spots. Corresponding isotopic values are shown in **C**. In **A**, a part of the crystal is not exposed in the cross-section, as indicated by the line.

4.3. U-Pb Geochronology

The only calcite sample yielding a robust U-Pb age determination was 178 m. The spatial correlation between the SIMS spots for stable isotopes and the U-Pb LA-ICP-MS spots shows that the dating represents the late karst calcite group in Figure 3a (most $\delta^{18}\text{O}$ values between -13‰ and -11‰ and $\delta^{13}\text{C}$ of -7‰ to -4‰), but not the outermost overgrowths. The LA-ICP-MS spots from a couple of different crystals within the late karst calcite population line up along two distinct regressions (Figure 6), with ages of 9.6 ± 1.3 Ma (MSWD = 1.4) and 2.5 ± 0.2 Ma (MSWD = 0.9). Each of these regressions represents several spots from multiple crystals, but each crystal only conforms to one of the ages. The latest calcite overgrowth and the older crystal cores were not targeted in this sample due to the small size of the crystal domains of these groups.

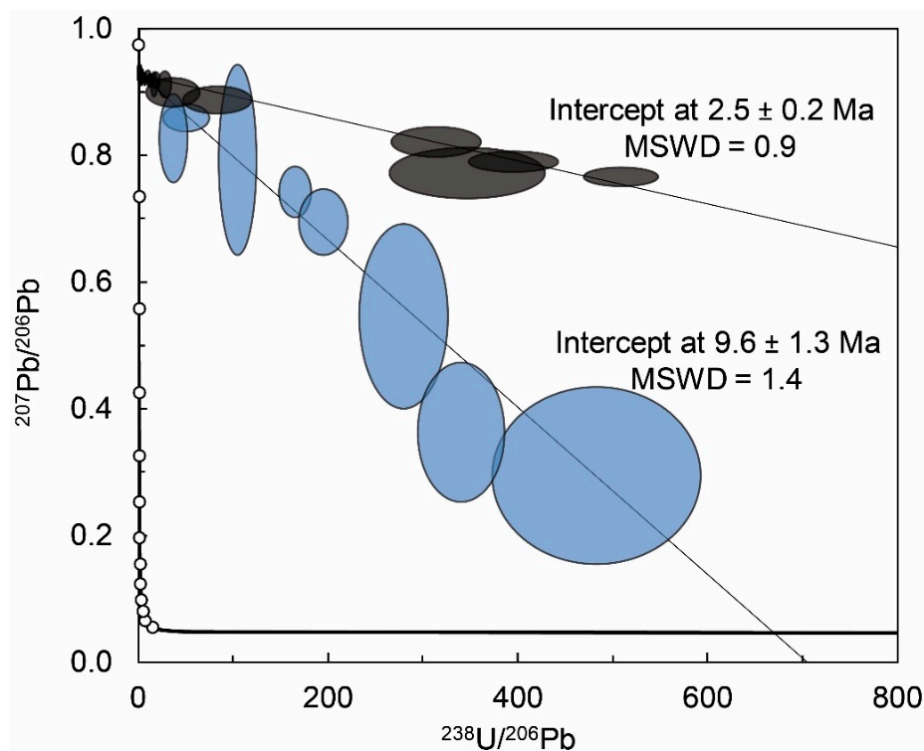


Figure 6. U-Pb dating of calcite sample 178 m, ages reflect non-anchored lower intercept ages and uncertainties are quoted at 2 s and comprise systematic uncertainties. Spot locations and details are reported in Supplementary Table S4 and Figure S4.

5. Discussion

The different populations of isotope compositions in the mineral veins and micro-karst precipitates suggests several discrete events of precipitation and fluid circulation in the fracture system of the thrust sheets.

5.1. Microbial Activity

Microbial activity typically results in distinguishable C isotopic excursions [15] that can be traced in authigenic carbonate minerals [10,55]. The samples in this study show very moderate C-isotope variations, especially compared to fracture coatings from other sites on the Fennoscandian shield [26,28,56]. The C isotope signatures in the calcites of the COSC-1 core are thus no strong marker for microbial activity in situ, at least not for processes involving methane formation or oxidation, which are known to produce carbonates strongly enriched in ^{13}C or depleted in ^{13}C , respectively [8,15,55,57], as documented elsewhere on the Fennoscandian shield [26,28,29,58,59]. The moderate $\delta^{13}\text{C}$ -depletion that is observed may, however, reflect the influence of C originating from dissolved organic carbon that has been oxidized by microbial communities and then mixed with less ^{13}C -depleted dissolved inorganic carbon in the waters. The C isotope composition of calcite reflects the result of several (cryptic) potential processes, and interpretations of $\delta^{13}\text{C}$ compositions in the observed span are not straightforward without additional evidence. Remnants of a biofilm occur on the karst cavity walls in sample 122 (Figure S3) and is another indication of microbial activity. The SEM-EDS analysis confirmed a carbonaceous composition, but the sample volume of the biofilm was too small for biomarker analysis, which could have offered further information about what communities inhabited this cavity. The small variation and small depletion in $\delta^{13}\text{C}$ values of the two deepest samples, suggest very small, if any, influence from microbial activity here and formation from a single precipitation event and fluid source, in contrast to the shallower samples (Figure 3c).

The generally large fractionation of the stable sulfur isotopes associated with microbial sulfate reduction, due to faster turnover of ^{32}S than ^{34}S [60], thus leading to discrimination of ^{34}S , has made this isotope system one of the most extensively used for understanding both modern and ancient biogeochemical cycles [61,62]. Laboratory culture measurements have reported sulfur isotope enrichments ($\delta^{34}\text{S}_{\text{sulfate-sulfide}}$ or $^{34}\epsilon$) as large as 66‰ [63] but even larger have been inferred from natural observations [64–66].

The low minimum $\delta^{34}\text{S}_{\text{pyrite}}$ values ($-19.8\text{‰} \pm 1.6\text{‰}$) in the young pyrite population reflect ^{32}S enrichment in the produced sulfide during MSR in the micro-karst. The initial sulfate $\delta^{34}\text{S}$ composition is unknown, but ambient water within the Fennoscandian Shield at other sites have $\delta^{34}\text{S}_{\text{SO}_4}$ values in the +15‰ to +25‰ range [67], which implies an isotope enrichment, $^{34}\epsilon$ ($\delta^{34}\text{S}_{\text{SO}_4} - \delta^{34}\text{S}_{\text{pyrite}}$), of 35–45‰ if we assumed pyrite in the studied fractures formed from water of similar $\delta^{34}\text{S}_{\text{SO}_4}$ composition. This $^{34}\epsilon$ is fully in line with MSR [66]. This younger generation of pyrite is related to the second and dominant calcite in the micro-karst at 178 m. A calcite generation that gave two different ages for two grain populations (2.5 ± 0.2 Ma and 9.6 ± 1.3 Ma) which thus also represents the age span of this MSR-related pyrite generation. The relatively narrow span in values for this pyrite suggests that it formed under open system conditions because there is no indication of successively increasing values with growth, which is a typical feature of Rayleigh isotope fractionation at closed or semi-closed conditions for sulfate [12].

The older pyrite generation in the micro-karst (dominating in sample at 122 m depth) showing more ^{34}S -enriched values can be thermochemical in origin, as this process generally does not involve significant degrees of fractionation [16,68]. Alternatively, the $\delta^{34}\text{S}$ values of this generation can reflect a late stage MSR-system undergoing Rayleigh fractionation in a semi-closed system, but this requires that significant amounts of isotopically light sulfide has been produced and precipitated elsewhere along the flow path [14].

5.2. Paleo-Fluid Flow and Water Types

The O isotope composition of the calcite crystals and veins can provide information about the fluid source. Unfortunately, there is no hydrochemical data available from the deep fractures in the COSC-1 borehole for comparison. Instead, we compare our determined $\delta^{18}\text{O}$ values with model glacial and meteoric waters at ambient temperatures, taking into account the temperature-dependent O-isotope fractionation that occurs during calcite precipitation (Figure 3a, [22]). For the late micro-karst precipitates, there is no temperature estimate available due to the fact that no two-phased fluid inclusions could be detected. This feature points to fluid inclusion entrapment at temperatures below 50 °C [69], and the detection of coeval MSR-related $\delta^{34}\text{S}_{\text{pyrite}}$ values also is in favor of low-temperature formation. If we assign a hypothetical meteoric water ($\delta^{18}\text{O}$: -11.5‰ to -9.5‰ SMOW) based on modern precipitation in Sweden [67] and formation temperatures of 5 to 20 °C, it is in accordance with the composition of the 2.5 ± 0.2 / 9.6 ± 1.3 Ma micro-karst calcite (Figure 3a). This means that precipitation of this calcite from a meteoric water is possible. However, it should be noted that in high latitude terrains, the $\delta^{18}\text{O}$ values can be even lighter than those we assigned [70]. This period of fluid flow and mineral growth in the micro-karst is temporally related to late Oligocene to Pliocene continental uplift of Fennoscandia [71] and the present relief of the Caledonides is largely the result of uplift during these times [35] with subsequent glacial-erosion modification [34].

The $\delta^{18}\text{O}$ composition of glacial meltwater from Pleistocene ice sheets in Fennoscandia has been estimated to a range of -22‰ to -20‰ [72], but recent studies of sub-ice sheet runoff at western Greenland show even more depleted values. When assigning a hypothetical glacial water with $\delta^{18}\text{O}$ of -27‰ to -20‰ SMOW, and temperatures of 5–10 °C, the temperature dependent fractionation results in modeled values in calcite of c. -26‰ to -18‰ V-PDB (Figure 3a), which is significantly lighter than the young micro-karst calcite, but in line with the early micro-karst and vein calcite. This means that it is unlikely that the young micro-karst calcite precipitated from a glacial water, but that the older calcite and veins may be glacial precipitates. However, if we assign a brine with similar composition as at

Sellafield ($\delta^{18}\text{O}$: -5‰ SMOW [73], Figure 1) and higher formation temperatures (100–150 °C), we will end up with hypothetical calcite with $\delta^{18}\text{O}$ values (c. -23 to -19 V-PDB) that also match the most ^{18}O -rich precipitates of these calcite groups. Furthermore, the mineralogical assemblage of the veins, with minerals such as epidote and laumontite, that are not formed at ambient temperatures [74,75], also speak against low-temperature formation from glacial water. For future studies, we suggest that the clumped isotope methodology is utilized for COSC-veins in order to potentially obtain formation temperature estimates of the carbonates. This approach has recently been proven successful to determine calcite precipitation temperatures in veins and constrain fluid sources, and fluxes, e.g., in the Peak District, UK [76]. Taken together, the calcites can be divided into groups based on their isotopic composition (mainly decided on $\delta^{18}\text{O}$) of which the veins seems to be of higher temperature type based on the presence of epidote and laumontite. The young micro-karst calcite was the only group that was dated ($2.5 \pm 0.2 / 9.6 \pm 1.3$ Ma) and overlaps with a low-temperature meteoric water. There is also an even younger group of overgrowths (i.e., younger than 2.5 ± 0.2 Ma) with lower $\delta^{13}\text{C}$ values than the dated calcite, but the overgrowths were too small for U-Pb LA-ICP-MS dating.

6. Conclusions

We present a microanalysis study (SIMS and LA-ICP-MS) recording ancient secondary mineral formation, fluid flow and microbial activity in a nappe unit of the Scandinavian Caledonides (utilizing the deep COSC-1 borehole). Petrographic and isotopic evidence for several generations of calcite and pyrite growth in micro-karst are determined. ^{34}S -depleted composition of pyrite suggests formation following microbial sulfate reduction in the karst and the O isotope composition of coeval calcite dated to $2.5 \pm 0.2 / 9.6 \pm 1.3$ Ma overlap with low-temperature meteoric water, in contrast to older calcite that has significantly lower $\delta^{18}\text{O}$ values. Our results mark the potential of combined SIMS and LA-ICP-MS micro-analysis within fine-grained mineral grains to understand and temporally determine discrete events of fluid flow and microbial activity in deep fracture systems and karsts of mountain ranges.

Supplementary Materials: The following are available online at <http://www.mdpi.com/2076-3263/10/2/56/s1>: Table S1: SIMS analyses of C isotopes in calcite and matrix matched reference material; Table S2: SIMS analyses of O isotopes in calcite and matrix matched reference material; Table S3: SIMS analyses of S isotopes in pyrite and matrix matched reference material; Table S4: LA-ICP-MS analyses for U-Pb calcite geochronology of sample 178 and matrix matched reference materials. Table S5: Sample photo documentation. Table S6: Sample details. Supplementary Figures S1–S4 with captions; Figure S1. Core log with mineral samples marked. This log is based on on-site descriptions, and the depth is subject to minor corrections post-drilling (this file is adopted from the ‘operation datasets’ for COSC-1, <http://dataservices.gfz-potsdam.de/icdp/showshort.php?id=escidoc:1095929>). Figure S2. Back-scattered SEM-images showing (A) aggregates of calcite crystals on the walls of micro-karst cavities of sample 122 m depth, (B) Euhedral and partly intergrown crystals of chabazite and calcite on the walls of micro-karst cavities of sample 178 m depth. Chabazite is slightly darker and not as fine-grained as calcite. (C) Euhedral and partly intergrown crystals of chabazite and calcite on the walls of micro-karst cavities of sample 178 m depth. (D) Euhedral and partly intergrown crystals of clay minerals (radiating aggregate of platy crystals), chabazite and calcite on the walls of micro-karst cavities of sample 178 m depth. (E) Vein assemblage of calcite, chlorite and Ti-oxide in polished block of sample 684 m. (F) Vein assemblage of calcite and laumontite (darker grey than calcite) in polished block of sample 743 m. Note that laser-ablation spots (visible) for dating tries have altered the sample slightly (darker areas). (G) Vein assemblage of calcite, pyrrhotite, quartz and epidote in polished block of sample 1369 m. (H) Vein assemblage of calcite, albite and ilmenite in polished block of sample 2210 m. Figure S3. Back-scattered SEM-images showing remnants of biofilm (carbonaceous matter) on the walls of micro-karst cavities of sample 122.8 m depth. Figure S4. Spot locations for LA-ICP-MS U-Pb geochronology analyses in polished calcite grains of sample 178 m, numbers and colors correspond to analytical details in Table S4.

Author Contributions: Conceptualization, H.D. and N.M.W.R.; methodology, and formal analysis, H.D. N.M.W.R. and M.J.W.; investigation, H.D. and N.M.W.R. writing—original draft preparation, H.D. and N.M.W.R.; writing—review and editing, H.D., N.M.W.R. and M.J.W.; visualization, H.D. and N.M.W.R.; funding acquisition, H.D., N.M.W.R. and M.J.W. All authors have read and agreed to the published version of the manuscript.

Funding: This research was funded by Swedish research council (contract 2017-05186 to H.D.) and Formas (contract 2017-00766 to H.D. and M.J.W.). The Natural Environment Research Council provides financial support of the Geochronology and Tracers Facility, British Geological Survey. NordSIM is part of the NordSIM-Vegacenter infrastructure supported by the Swedish Research Council grant 2017-00637. COSC-1 was drilled within the Swedish national research infrastructure for scientific drilling “Riksriggen” and financed by the International Continental Scientific Drilling Program (ICDP) and the Swedish Research Council.

Acknowledgments: K. Lindén and H. Jeon are thanked for analytical and/or sample preparation assistance. M. Konrad-Schmolke at University of Gothenburg is thanked for SEM analysis access. H. Lorenz provided visualization support. N.M.W.R. thanks the British Geological Survey for funding to sample the core, and John Fletcher for sample preparation. This is NordSIM publication 630.

Conflicts of Interest: The authors declare no conflict of interest.

References

1. De Graaf, S.; Lüders, V.; Banks, D.A.; Sośnicka, M.; Reijmer, J.J.; Kaden, H.; Vonhof, H.B. Fluid evolution and ore deposition in the Harz Mountains revisited: Isotope and crush-leach analyses of fluid inclusions. *Miner. Depos.* **2019**, *1*–16. [[CrossRef](#)]
2. Ivarsson, M.; Kiliyas, S.P.; Broman, C.; Neubeck, A.; Drake, H.; Fru, E.C.; Bengtson, S.; Naden, J.; Detsi, K.; Whitehouse, M.J. Exceptional Preservation of Fungi as H₂-Bearing Fluid Inclusions in an Early Quaternary Paleo-Hydrothermal System at Cape Vani, Milos, Greece. *Minerals* **2019**, *9*, 749. [[CrossRef](#)]
3. Dexter-Dyer, B.; Kretzschmar, M.; Krumbein, W.E. Possible microbial pathways in the formation of Precambrian ore deposits. *J. Geol. Soc.* **1984**, *141*, 251–262. [[CrossRef](#)]
4. Martini, A.M.; Budai, J.M.; Walter, L.M.; Schoell, M. Microbial generation of economic accumulations of methane within a shallow organic-rich shale. *Nature* **1996**, *383*, 155–158. [[CrossRef](#)]
5. Drake, H.; Roberts, N.M.W.; Heim, C.; Whitehouse, M.J.; Siljeström, S.; Kooijman, E.; Broman, C.; Ivarsson, M.; Åström, M.E. Timing and origin of natural gas accumulation in the Siljan impact structure, Sweden. *Nat. Commun.* **2019**, *10*, 4736. [[CrossRef](#)] [[PubMed](#)]
6. Tullborg, E.-L.; Drake, H.; Sandström, B. Palaeohydrogeology: A methodology based on fracture mineral studies. *Appl. Geochem.* **2008**, *23*, 1881–1897. [[CrossRef](#)]
7. Sahlstedt, E.; Karhu, J.A.; Pitkänen, P. Indications for the past redox environments in deep groundwaters from the isotopic composition of carbon and oxygen in fracture calcite, Olkiluoto, SW Finland. *Isot. Environ. Heal. Stud.* **2010**, *46*, 370–391. [[CrossRef](#)] [[PubMed](#)]
8. Budai, J.M.; Walter, L.M.; Ku, T.C.W.; Martini, A.M. Fracture-fill calcite as a record of microbial methanogenesis and fluid migration: A case study from the Devonian Antrim Shale, Michigan Basin. *Geofluids* **2002**, *2*, 163–183. [[CrossRef](#)]
9. Feng, D.; Chen, D.; Peckmann, J.; Bohrmann, G. Authigenic carbonates from methane seeps of the northern Congo fan: Microbial formation mechanism. *Mar. Pet. Geol.* **2010**, *27*, 748–756. [[CrossRef](#)]
10. Natalicchio, M.; Birgel, D.; Pierre, F.D.; Martire, L.; Clari, P.; Spötl, C.; Peckmann, J. Polyphasic carbonate precipitation in the shallow subsurface: Insights from microbially-formed authigenic carbonate beds in upper Miocene sediments of the Tertiary Piedmont Basin (NW Italy). *Palaeogeogr. Palaeoclim. Palaeoecol.* **2012**, *329*, 158–172. [[CrossRef](#)]
11. Caesar, K.H.; Kyle, J.R.; Lyons, T.W.; Tripathi, A.; Loyd, S.J. Carbonate formation in salt dome cap rocks by microbial anaerobic oxidation of methane. *Nat. Commun.* **2019**, *10*, 808. [[CrossRef](#)] [[PubMed](#)]
12. Kohn, M.J.; Riciputi, L.R.; Stakes, D.; Orange, D.L. Sulfur isotope variability in biogenic pyrite; reflections of heterogeneous bacterial colonization? *Am. Mineral.* **1998**, *83*, 1454–1468. [[CrossRef](#)]
13. Parnell, J.; Boyce, A.; Thackrey, S.; Muirhead, D.; Lindgren, P.; Mason, C.; Taylor, C.; Still, J.; Bowden, S.; Osinski, G.R.; et al. Sulfur isotope signatures for rapid colonization of an impact crater by thermophilic microbes. *Geology* **2010**, *38*, 271–274. [[CrossRef](#)]
14. Drake, H.; Whitehouse, M.J.; Heim, C.; Reiners, P.W.; Tillberg, M.; Hogmalm, K.J.; Dopson, M.; Broman, C.; Åström, M.E. Unprecedented 34 S-enrichment of pyrite formed following microbial sulfate reduction in fractured crystalline rocks. *Geobiology* **2018**, *16*, 556–574. [[CrossRef](#)]
15. Knittel, K.; Boetius, A. Anaerobic Oxidation of Methane: Progress with an Unknown Process. *Annu. Rev. Microbiol.* **2009**, *63*, 311–334. [[CrossRef](#)]
16. Machel, H.G.; Krouse, H.R.; Sassen, R. Products and distinguishing criteria of bacterial and thermochemical sulfate reduction. *Appl. Geochem.* **1995**, *10*, 373–389. [[CrossRef](#)]
17. Drake, H.; Tullborg, E.-L. Paleohydrogeological events recorded by stable isotopes, fluid inclusions and trace elements in fracture minerals in crystalline rock, Simpevarp area, SE Sweden. *Appl. Geochem.* **2009**, *24*, 715–732. [[CrossRef](#)]

18. Blyth, A.; Frape, S.; Ruskeeniemi, T.; Blomqvist, R. Origins, closed system formation and preservation of calcites in glaciated crystalline bedrock: Evidence from the Palmottu natural analogue site, Finland. *Appl. Geochem.* **2004**, *19*, 675–686. [[CrossRef](#)]
19. Mathurin, F.A.; Åström, M.E.; Laaksoharju, M.; Kalinowski, B.E.; Tullborg, E.-L. Effect of Tunnel Excavation on Source and Mixing of Groundwater in a Coastal Granitoidic Fracture Network. *Environ. Sci. Technol.* **2012**, *46*, 12779–12786. [[CrossRef](#)]
20. O’Neil, J.R. Oxygen Isotope Fractionation in Divalent Metal Carbonates. *J. Chem. Phys.* **1969**, *51*, 5547. [[CrossRef](#)]
21. Watkins, J.M.; Hunt, J.D.; Ryerson, F.J.; DePaolo, D.J. The influence of temperature, pH, and growth rate on the $\delta^{18}\text{O}$ composition of inorganically precipitated calcite. *Earth Planet. Sci. Lett.* **2014**, *404*, 332–343. [[CrossRef](#)]
22. Kim, S.-T.; O’Neil, J.R. Equilibrium and nonequilibrium oxygen isotope effects in synthetic carbonates. *Geochim. Cosmochim. Acta* **1997**, *61*, 3461–3475. [[CrossRef](#)]
23. Drake, H.; Ivarsson, M.; Tillberg, M.; Whitehouse, M.J.; Kooijman, E. Ancient Microbial Activity in Deep Hydraulically Conductive Fracture Zones within the Forsmark Target Area for Geological Nuclear Waste Disposal, Sweden. *Geosciences* **2018**, *8*, 211. [[CrossRef](#)]
24. Drake, H.; Ivarsson, M.; Bengtson, S.; Heim, C.; Siljeström, S.; Whitehouse, M.J.; Broman, C.; Belivanova, V.; Åström, M.E. Anaerobic consortia of fungi and sulfate reducing bacteria in deep granite fractures. *Nat. Commun.* **2017**, *8*, 55. [[CrossRef](#)]
25. Drake, H.; Åström, M.E.; Tullborg, E.-L.; Whitehouse, M.; Fallick, A.E. Variability of sulphur isotope ratios in pyrite and dissolved sulphate in granitoid fractures down to 1km depth—Evidence for widespread activity of sulphur reducing bacteria. *Geochim. Cosmochim. Acta* **2013**, *102*, 143–161. [[CrossRef](#)]
26. Sahlstedt, E.; Karhu, J.A.; Pitkänen, P.; Whitehouse, M. Biogenic processes in crystalline bedrock fractures indicated by carbon isotope signatures of secondary calcite. *Appl. Geochem.* **2016**, *67*, 30–41. [[CrossRef](#)]
27. Sahlstedt, E.; Karhu, J.; Pitkanen, P.; Whitehouse, M. Implications of sulfur isotope fractionation in fracture-filling sulfides in crystalline bedrock, Olkiluoto, Finland. *Appl. Geochem.* **2013**, *32*, 52–69. [[CrossRef](#)]
28. Drake, H.; Heim, C.; Roberts, N.M.; Zack, T.; Tillberg, M.; Broman, C.; Ivarsson, M.; Whitehouse, M.J.; Åström, M.E. Isotopic evidence for microbial production and consumption of methane in the upper continental crust throughout the Phanerozoic eon. *Earth Planet. Sci. Lett.* **2017**, *470*, 108–118. [[CrossRef](#)]
29. Drake, H.; Åström, M.E.; Heim, C.; Broman, C.; Åström, J.; Whitehouse, M.; Ivarsson, M.; Siljeström, S.; Sjövall, P. Extreme ^{13}C depletion of carbonates formed during oxidation of biogenic methane in fractured granite. *Nat. Commun.* **2015**, *6*, 7020. [[CrossRef](#)]
30. Lorenz, H.; Rosberg, J.-E.; Juhlin, C.; Bjelm, L.; Almquist, B.S.G.; Berthet, T.; Conze, R.; Gee, D.G.; Klonowska, I.; Pascal, C.; et al. COSC-1 – drilling of a subduction-related allochthon in the Palaeozoic Caledonide orogen of Scandinavia. *Sci. Drill.* **2015**, *19*, 1–11. [[CrossRef](#)]
31. Gee, D.G.; Juhlin, C.; Pascal, C.; Robinson, P. Collisional Orogeny in the Scandinavian Caledonides (COSC). *GFF* **2010**, *132*, 29–44. [[CrossRef](#)]
32. Corfu, F.; Andersen, T.B.; Gasser, D. The Scandinavian Caledonides: Main features, conceptual advances and critical questions. *Geol. Soc. Lond. Spec. Publ.* **2014**, *390*, 9–43. [[CrossRef](#)]
33. Roberts, D. The Scandinavian Caledonides: Event chronology, palaeogeographic settings and likely modern analogues. *Tectonophysics* **2003**, *365*, 283–299. [[CrossRef](#)]
34. Lidmar-Bergström, K.; Näslund, J.O.; Ebert, K.; Neubeck, T.; Bonow, J.M. Cenozoic landscape development on the passive margin of northern Scandinavia. *Nor. J. Geol.* **2007**, *87*, 181–196.
35. Lidmar-Bergström, K. Long term morphotectonic evolution in Sweden. *Geomorphology* **1996**, *16*, 33–59. [[CrossRef](#)]
36. Kendrick, M.; Burgess, R.; Harrison, D.; Bjørlykke, A. Noble gas and halogen evidence for the origin of Scandinavian sandstone-hosted Pb-Zn deposits. *Geochim. Cosmochim. Acta* **2005**, *69*, 109–129. [[CrossRef](#)]
37. Hedin, P.; Almquist, B.; Berthet, T.; Juhlin, C.; Buske, S.; Simon, H.; Giese, R.; Krauß, F.; Rosberg, J.-E.; Alm, P.-G. 3D reflection seismic imaging at the 2.5km deep COSC-1 scientific borehole, central Scandinavian Caledonides. *Tectonophysics* **2016**, *689*, 40–55. [[CrossRef](#)]
38. Lorenz, H.; Rosberg, J.E.; Juhlin, C.; Bjelm, L.; Almquist, B.G.S.; Berthet, T.; Conze, R.; Gee, D.; Klonowska, I.; Pascal, C.; et al. Operational report about phase 1 of the Collisional Orogeny in the Scandinavian Caledonides scientific drilling project (COSC-1). *ICDP Oper. Rep. Potsdam GFZ Ger. Res. Cent. Geosci.* **2015**, *52*.

39. Roberts, D.; Gee, D.G. An introduction to the structure of the Scandinavian Caledonides. *Caledonide Orogen–Scand. Relat. Areas* **1985**, *1*, 55–68.
40. Andréasson, P.-G.; Gorbatshev, R. Metamorphism in extensive nappe terrains: A study of the Central Scandinavian Caledonides. *Geologiska Föreningen i Stockholm Förhandlingar* **1980**, *102*, 335–357. [[CrossRef](#)]
41. Be’Eri-Shlevin, Y.; Gee, D.; Claesson, S.; Ladenberger, A.; Majka, J.; Kirkland, C.; Robinson, P.; Frei, D. Provenance of Neoproterozoic sediments in the Särvi nappes (Middle Allochthon) of the Scandinavian Caledonides: LA-ICP-MS and SIMS U–Pb dating of detrital zircons. *Precambrian Res.* **2011**, *187*, 181–200. [[CrossRef](#)]
42. Gee, D.G.; Fossen, H.; Henriksen, N.; Higgins, A.K. From the Early Paleozoic Platforms of Baltica and Laurentia to the Caledonide Orogen of Scandinavia and Greenland. *Episodes* **2008**, *31*, 44–51. [[CrossRef](#)] [[PubMed](#)]
43. Ladenberger, A.; Be’eri-Shlevin, Y.; Claesson, S.; Gee, D.G.; Majka, J.; Romanova, I.V. Tectonometamorphic evolution of the Åreskutan Nappe–Caledonian history revealed by SIMS U–Pb zircon geochronology. *Geol. Soc. Lond. Spec. Publ.* **2014**, *390*, 337–368. [[CrossRef](#)]
44. Gromet, L.; Sjöström, H.; Bergman, S.; Claesson, S.; Essex, R.; Andréasson, P.; Albrecht, L. Contrasting ages of metamorphism in the Seve nappes: U–Pb results from the central and northern Swedish Caledonides. *GFF* **1996**, *118*, 36–37. [[CrossRef](#)]
45. Williams, I.S.; Claesson, S. Isotopic evidence for the Precambrian provenance and Caledonian metamorphism of high grade paragneisses from the Seve Nappes, Scandinavian Caledonides. *Contrib. Mineral. Petrol.* **1987**, *97*, 205–217. [[CrossRef](#)]
46. Bender, H.; Glodny, J.; Ring, U. Absolute timing of Caledonian orogenic wedge assembly, Central Sweden, constrained by Rb–Sr multi-mineral isochron data. *Lithos* **2019**, *344–345*, 339–359. [[CrossRef](#)]
47. Klonowska, I.; Janák, M.; Majka, J.; Petřík, I.; Froitzheim, N.; Gee, D.G.; Sasinková, V. Microdiamond on Åreskutan confirms regional UHP metamorphism in the Seve Nappe Complex of the Scandinavian Caledonides. *J. Metamorph. Geol.* **2017**, *35*, 541–564. [[CrossRef](#)]
48. Tsang, C.-F.; Rosberg, J.-E.; Sharma, P.; Berthet, T.; Juhlin, C.; Niemi, A. Hydrologic testing during drilling: Application of the flowing fluid electrical conductivity (FFEC) logging method to drilling of a deep borehole. *Hydrogeol. J.* **2016**, *24*, 1333–1341. [[CrossRef](#)]
49. Kamber, B.S.; Whitehouse, M.J. Micro-scale sulphur isotope evidence for sulphur cycling in the late Archean shallow ocean. *Geobiology* **2007**, *5*, 5–17. [[CrossRef](#)]
50. Ding, T.; Valkiers, S.; Kipphardt, H.; De Bièvre, P.; Taylor, P.; Gonfiantini, R.; Krouse, R. Calibrated sulfur isotope abundance ratios of three IAEA sulfur isotope reference materials and V-CDT with a reassessment of the atomic weight of sulfur. *Geochim. Cosmochim. Acta* **2001**, *65*, 2433–2437. [[CrossRef](#)]
51. Roberts, N.M.W.; Rasbury, E.T.; Parrish, R.R.; Smith, C.J.; Horstwood, M.S.A.; Condon, D.J. A calcite reference material for LA-ICP-MS U–Pb geochronology. *Geochem. Geophys. Geosystems* **2017**, *18*, 2807–2814. [[CrossRef](#)]
52. Ludwig, K. Isoplot version 4.15: A geochronological toolkit for microsoft Excel. *Berkeley Geochronol. Cent. Spec. Publ.* **2008**, *4*, 247–270.
53. Hill, C.A.; Polyak, V.J.; Asmerom, Y.; Provencio, P.P. Constraints on a Late Cretaceous uplift, denudation, and incision of the Grand Canyon region, southwestern Colorado Plateau, USA, from U–Pb dating of lacustrine limestone. *Tectonics* **2016**, *35*, 896–906. [[CrossRef](#)]
54. Horstwood, M.S.A.; Kosler, J.; Gehrels, G.; Jackson, S.E.; McLean, N.M.; Paton, C.; Pearson, N.J.; Sircombe, K.; Sylvester, P.; Vermeesch, P.; et al. Community-Derived Standards for LA-ICP-MS U–(Th–)Pb Geochronology—Uncertainty Propagation, Age Interpretation and Data Reporting. *Geostand. Geoanalytical Res.* **2016**, *40*, 311–332. [[CrossRef](#)]
55. Peckmann, J.; Thiel, V. Carbon cycling at ancient methane–seeps. *Chem. Geol.* **2004**, *205*, 443–467. [[CrossRef](#)]
56. Sandström, B.; Tullborg, E.-L. Episodic fluid migration in the Fennoscandian Shield recorded by stable isotopes, rare earth elements and fluid inclusions in fracture minerals at Forsmark, Sweden. *Chem. Geol.* **2009**, *266*, 126–142. [[CrossRef](#)]
57. Campbell, K.; Farmer, J.D.; Marais, D.D. Ancient hydrocarbon seeps from the Mesozoic convergent margin of California: Carbonate geochemistry, fluids and palaeoenvironments. *Geofluids* **2002**, *2*, 63–94. [[CrossRef](#)]
58. Tullborg, E.-L.; Landström, O.; Wallin, B. Low-temperature trace element mobility influenced by microbial activity—Indications from fracture calcite and pyrite in crystalline basement. *Chem. Geol.* **1999**, *157*, 199–218. [[CrossRef](#)]

59. Clauer, N.; Frapé, S.K.; Fritz, B. Calcite veins of the Stripa granite (Sweden) as records of the origin of the groundwaters and their interactions with the granitic body. *Geochim. Cosmochim. Acta* **1989**, *53*, 1777–1781. [[CrossRef](#)]
60. Canfield, D. Isotope fractionation by natural populations of sulfate-reducing bacteria. *Geochim. Cosmochim. Acta* **2001**, *65*, 1117–1124. [[CrossRef](#)]
61. Ries, J.B.; Fike, D.A.; Pratt, L.M.; Lyons, T.W.; Grotzinger, J.P. Superheavy pyrite ($\delta^{34}\text{S}_{\text{pyr}} > \delta^{34}\text{S}_{\text{SCAS}}$) in the terminal Proterozoic Nama Group, southern Namibia: A consequence of low seawater sulfate at the dawn of animal life. *Geology* **2009**, *37*, 743–746. [[CrossRef](#)]
62. Jones, D.S.; Fike, D.A. Dynamic sulfur and carbon cycling through the end-Ordovician extinction revealed by paired sulfate–pyrite $\delta^{34}\text{S}$. *Earth Planet. Sci. Lett.* **2013**, *363*, 144–155. [[CrossRef](#)]
63. Sim, M.S.; Bosak, T.; Ono, S. Large Sulfur Isotope Fractionation Does Not Require Disproportionation. *Sci.* **2011**, *333*, 74–77. [[CrossRef](#)] [[PubMed](#)]
64. Wortmann, U.G.; Bernasconi, S.M.; Böttcher, M.E. Hypersulfidic deep biosphere indicates extreme sulfur isotope fractionation during single-step microbial sulfate reduction. *Geology* **2001**, *29*, 647. [[CrossRef](#)]
65. Drake, H.; Tullborg, E.-L.; Whitehouse, M.; Sandberg, B.; Blomfeldt, T.; Åström, M.E. Extreme fractionation and micro-scale variation of sulphur isotopes during bacterial sulphate reduction in deep groundwater systems. *Geochim. Cosmochim. Acta* **2015**, *161*, 1–18. [[CrossRef](#)]
66. Canfield, D.E.; Farquhar, J.; Zerkle, A.L. High isotope fractionations during sulfate reduction in a low-sulfate euxinic ocean analog. *Geology* **2010**, *38*, 415–418. [[CrossRef](#)]
67. Laaksoharju, M.; Smellie, J.; Tullborg, E.-L.; Gimeno, M.; Molinero, J.; Gurban, I.; Hallbeck, L. Hydrogeochemical evaluation and modelling performed within the Swedish site investigation programme. *Appl. Geochem.* **2008**, *23*, 1761–1795. [[CrossRef](#)]
68. Machel, H. Bacterial and thermochemical sulfate reduction in diagenetic settings—Old and new insights. *Sediment. Geol.* **2001**, *140*, 143–175. [[CrossRef](#)]
69. Goldstein, R.H. Fluid inclusions in sedimentary and diagenetic systems. *Lithos* **2001**, *55*, 159–193. [[CrossRef](#)]
70. Johansson, E.; Gustafsson, L.-G.; Berglund, S.; Lindborg, T.; Selroos, J.-O.; Liljedahl, L.C.; Destouni, G. Data evaluation and numerical modeling of hydrological interactions between active layer, lake and talik in a permafrost catchment, Western Greenland. *J. Hydrol.* **2015**, *527*, 688–703. [[CrossRef](#)]
71. Stuevold, L.M.; Eldholm, O. Cenozoic uplift of Fennoscandia inferred from a study of the mid-Norwegian margin. *Glob. Planet. Chang.* **1996**, *12*, 359–386. [[CrossRef](#)]
72. Pitkänen, P.; Partamies, S.; Luukkonen, A. *Hydrogeochemical Interpretation of Baseline Groundwater Conditions at the Olkiluoto Site*; Posiva Olkiluoto: Helsinki, Finland, 2004.
73. Milodowski, A.E.; Bath, A.; Norris, S. Palaeohydrogeology using geochemical, isotopic and mineralogical analyses: Salinity and redox evolution in a deep groundwater system through Quaternary glacial cycles. *Appl. Geochem.* **2018**, *97*, 40–60. [[CrossRef](#)]
74. Bird, D.K.; Spieler, A.R. Epidote in geothermal systems. *Rev. Mineral. Geochem.* **2014**, *56*, 235–300. [[CrossRef](#)]
75. Liou, J.G.; Maruyama, S.; Cho, M. Phase equilibria and mixed parageneses of metabasites in lowgrade metamorphism. *Mineral. Mag.* **1985**, *49*, 321–333. [[CrossRef](#)]
76. Dennis, P.F.; Myhill, D.J.; Marca, A.; Kirk, R. Clumped isotope evidence for episodic, rapid flow of fluids in a mineralized fault system in the Peak District, UK. *J. Geol. Soc.* **2019**, *176*, 447–461. [[CrossRef](#)]

